energies

MDPI

Article

The Effect of Distributed Parameters on Conducted EMI from DC-Fed Motor Drive Systems in Electric Vehicles

Li Zhai [1,2,*], Liwen Lin [1,2], Xinyu Zhang [3] and Chao Song [1,2]

[1] National Engineering Laboratory for Electric Vehicle, Beijing Institute of Technology, Beijing 100081, China; 15201430735@163.com (L.L.); 18210606506@163.com (C.S.)
[2] Co-Innovation Center of Electric Vehicles in Beijing, Beijing Institute of Technology, Beijing 100081, China
[3] Beijing Institute of Radio Metrology and Measurement, Beijing 100854, China; xinyuzhang203@163.com
* Correspondence: zhaili26@bit.edu.cn; Tel.: +86-10-6891-5202

Academic Editor: Joeri Van Mierlo
Received: 18 August 2016; Accepted: 12 December 2016; Published: 22 December 2016

Abstract: The large dv/dt and di/dt outputs of power devices in DC-fed motor drive systems in electric vehicles (EVs) always introduce conducted electromagnetic interference (EMI) emissions and may lead to motor drive system energy transmission losses. The effect of distributed parameters on conducted EMI from the DC-fed high voltage motor drive systems in EVs is studied. A complete test for conducted EMI from the direct current fed(DC-fed) alternating current (AC) motor drive system in an electric vehicle (EV) under load conditions is set up to measure the conducted EMI of high voltage DC cables and the EMI noise peaks due to resonances in a frequency range of 150 kHz–108 MHz. The distributed parameters of the motor can induce bearing currents under low frequency sine wave operation. However the impedance of the distributed parameters of the motor is very high at resonance frequencies of 500 kHz and 30 MHz, and the effect of the bearing current can be ignored, so the research mainly focuses on the distributed parameters in inverters and cables at 500 kHz and 30 MHz, not the effect of distributed parameters of the motor on resonances. The corresponding equivalent circuits for differential mode (DM) and common mode (CM) EMI at resonance frequencies of 500 kHz and 30 MHz are established to determine the EMI propagation paths and analyze the effect of distributed parameters on conducted EMI. The dominant distributed parameters of elements responsible for the appearing resonances at 500 kHz and 30 MHz are determined. The effect of the dominant distributed parameters on conducted EMI are presented and verified by simulation and experiment. The conduced voltage at frequencies from 150 kHz to 108 MHz can be mitigated to below the limit level-3 of CISPR25 by changing the dominant distributed parameters.

Keywords: electric vehicle; DC-fed; motor drive system; conducted electromagnetic interference (EMI); distributed parameter

1. Introduction

In the face of the worldwide demand for reduction in greenhouse gas emissions and $PM_{2.5}$ production [1], recently many countries have adopted policies, mainly in the form of tax incentives for the purchase, to increase the number of electric vehicles (EVs) and thus reduce pollutant emissions and improve the air quality, especially in urban areas [2–5]. Electromagnetic interference (EMI) considerations in EVs have become increasingly important, as the electromagnetic compatibility (EMC) regulations for EVs (typically defined from 10 kHz to 30 MHz) have become more stringent [6]. The DC-fed motor drive system of EVs, consisting of the electric motor, power inverter, and electronic controller has an essential role in EVs [7]. Large dv/dt and di/dt due to high-speed switching of power devices within a DC-fed voltage-type pulse width modulation (PWM) inverter of high-power-density

and high-efficiency motor drive system always introduce unwanted higher-order harmonics currents and high frequency noise currents through parasitic/distributed parameters of the motor system [8–10], and are mainly responsible for the conducted and/or radiated electromagnetic interference (EMI) emissions which will greatly affect the behavior of low voltage supply electronic equipment (such as board bus system, sensors, vehicle control units (VCUs), battery management systems (BMSs), power batteries, and the drive motor in EVs [6,11]. Additionally, the unwanted higher-order harmonics current from the motor drive system due to the switching of insulated gate bipolar transistors (IGBTs) can not only generate common mode (CM) EMI and differential mode (DM) EMI emissions, but also increase the motor losses, which may lead to energy transmission losses and thermal problems in the power inverter system.

1.1. Literature Review

Much valuable work involving the EMI emissions of the motor drive system for conventional industrial applications has been widely conducted by many researchers [12–14]. However, the EMI from the drive motor system under varying load conditions for EVs is different from that of a conventional industrial motor with no load or invariant load conditions. Previous studies on EMI emissions from vehicle components are based on the measurements specified in the EMC standard CISPR25 (International Special Committee on Radio Interference 25) [15,16], which are implemented for low voltage components in EVs and not suitable for the high voltage applications in EVs (e.g., motor system, charging system), so we cannot correctly predict the EMI emissions from the high voltage motor system in EVs due to the fact few EMC laboratories have the dynamometer needed to study EVs under varying loading conditions, so the present study on the EMI mechanism and propagation path of the motor system is much less than that on the total EMC performance of EVs [17,18]. The EMI emissions from the high voltage cables of the AC motor drive system of EVs under load condition have not been considered in previous works.

Various parasitics and distributed parameters exist inside the motor system and they play a very important role in the generation of EMI. The high-frequency leakage currents flowing to the ground could be generated through distributed parameters between the components of the motor drive system (such as the motor, inverter, cables, etc.) and the chassis of the body of the EV at high frequency, and introduce the radiation of power cables, shaft voltage and bearing currents in the motor [19,20]. Additionally the EMI emission peaks due to resonances caused by distributed parameters may cause some energy losses of the motor drive system and decrease the efficiency of the system [21–23], so the distributed parameters at high frequency in the system should not be neglected anymore for EVs. Therefore, the effect of the distributed parameters on EMI emissions is important for identification of EMI propagation paths and the critical distributed parameters of elements responsible for EMI, and mitigation of EMI emissions [24].

Models of the motor drive system are necessary to analyze and predict the EMI sources and propagation inside the motor drive system to find the elements responsible for the EMI. Since the most basic and widely applied full-wave models based on the "black box" approach cannot show the location of the noise source or the propagation path inside the motor power inverter [20,25], some terminal modeling techniques for a two-port network were proposed to predict the conducted EMI [14,21,26]. However, there has never been a theoretical analysis of the parasitic effects of the distributed parameters on EMI noise suppression. An equivalent simulation program with integrated circuit (SPICE)-based model is a better approach to find the parts and elements of the motor inverter system responsible for EMI [12] and analyze the effects of the distributed parameters on the EMI noise. A rather simple measurement-based SPICE model of the motor power inverter has been presented [12] to quickly identify the parts responsible for EMI and help predict resonances between the two ports of the motor power inverter by a straightforward correlation between the system geometry and the parasitic circuit elements [27]. A detailed analysis of current paths and the equivalent circuits at three important resonance frequencies have been presented to determine the EMI propagation path in the

motor drive system [6]. A combination of mitigation strategies was designed to mitigate the CM conducted emission by IGBT switching and the radiated emissions of AC cables.

Most of the above work focuses on analyses of CM and DM EMI propagation paths in the system based on a "black box" approach, terminal modeling techniques and SPICE-based models, which have not considered the effect of the distributed parameters of the high voltage motor drive system in EVs on EMI noise, so the previous equivalent circuits of the EMI could not be correctly proposed to accurately and effectively predict the actual source and propagation of the EMI in the system. The effects of the distributed parameters on the conducted EMI noise have not been adequately considered previously because of a lack of the modeling of the conducted EMI from the high voltage motor drive system with suitable parameters and better analysis methods.

1.2. Motivation and Innovation

This study proposes a new method to analyze the effect of distributed parameters on conducted EMI from the DC-fed high voltage motor drive systems in EVs. A complete test for conducted EMI emissions from the AC motor drive system of an EV under load conditions will be set up to measure the conducted EMI of high voltage DC cables and EMI noise peaks due to resonances in a frequency range of 150 kHz–108 MHz. The corresponding equivalent circuits for DM and CM EMI at the resonance frequencies of 500 kHz and 30 MHz are established to determine the EMI propagation paths and analyze the effect of distributed parameters on conducted EMI. The dominant distributed parameters of elements responsible for the resonances appearing at 500 kHz and 30 MHz will be determined. The effect of the dominant distributed parameters on conducted EMI will be verified by simulations and experiments.

1.3. Organization of the Paper

The organization of this study is as follows: Section 2 illustrates the structure of the complete test setup for conducted EMI emissions from the AC motor drive system of an EV. Then, the corresponding current paths and equivalent circuits of DM and CM EMI at resonance frequencies of 500 kHz and 30 MHz, and the effect of distributed parameters on CM EMI will be presented in Section 3. After that, the simulation verification and discussion will be illustrated in Section 4. The experiment verification will be discussed in Section 5. Finally, conclusions are provided in Section 6.

2. System Conducted Emission Measurement

2.1. Conducted EMI Emission Setup

The complete test setup for conducted EMI emissions from the DC-fed AC motor drive system on an EV in an EMI laboratory is shown in Figure 1 and mainly consists of a DC power supply such as a Li-ion battery, DC cables, a DC-fed voltage-type PWM three-phase power inverter, AC cables, and an AC motor. Measurements were performed to comply with the CISPR 25 standard which provides conducted EMI emission limits for vehicle components in a frequency range of 150 kHz to 108 MHz [28]. Two standard line impedance stabilization networks (LISNs) terminated with 50 Ω resistances provide DC power from a battery or DC power supply to the three-phase power inverter using two shielded cables (2 m). The power inverter with 330 V DC input is connected to a 50 kW/100 kW permanent magnet synchronous motor (PMSM) using three shielded cables (1 m). As required by the EMC regulations of CISPR 25, all components are connected to a large copper sheet as ground reference plane, except for the AC motor which is located on an insulated bench covered with ferrite material and connected to an electric dynamometer supplying a mechanical load. The output speed and torque of the AC motor can be measured by a meter between the dynamometer and the insulated output shaft of the AC motor. With this configuration, the total conducted EMI noise voltage signals in DC cables can be picked up by any one of the line impedance stabilization network (LISN) impedances connected to an EMI receiver [29].

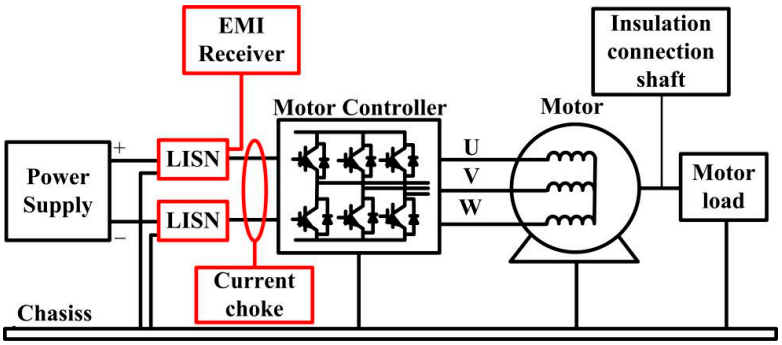

Figure 1. Conducted EMI emission system test setup for the AC motor drive system.

2.2. Conducted EMI Experiment Results

The AC motor is operated continuously at 2000 rpm speed with no-load and 60 N·m loaded torque, as shown in Figure 2. Figure 3 shows the experimental comparison in conducted EMI emission levels between the no-load and load conditions. This experimental result indicates that the conducted EMI noise voltage of the power inverter is dominant in a frequency range of 150 kHz to 108 MHz and is not compliant with CISPR25, as shown in Table 1. Therefore the conducted EMI emission levels in the load condition are more severe and higher than those in the no-load mode. Two noise voltage peaks at frequency around 500 kHz and 30 MHz can be observed and may mainly be caused by PWM switching harmonics or parasitic resonances due to the distributed parameters of the motor system [30]. It is critical to analyze the source and propagation mechanism of EMI to predict the conducted EMI emissions and determine the dominant distributed parameters of the elements in the motor system responsible for the resonances.

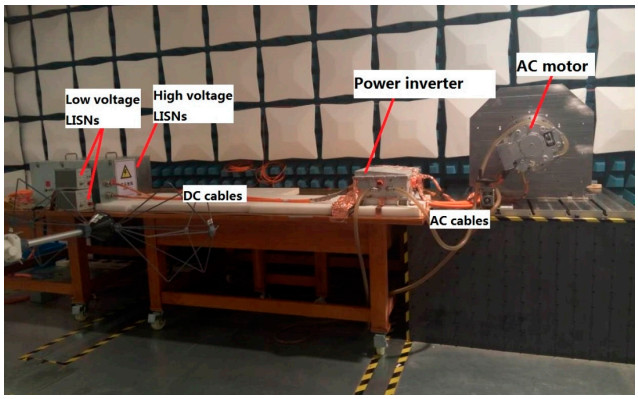

Figure 2. The test platform for conducted EMI emission.

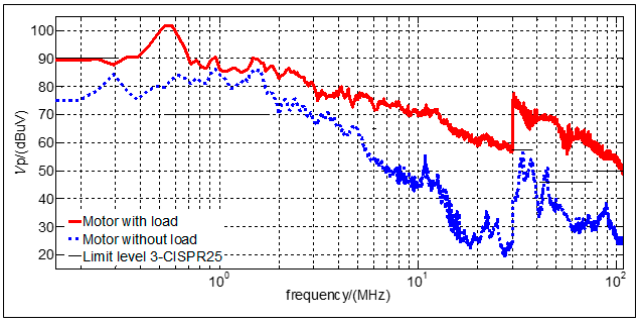

Figure 3. Comparison of measurement with load and measurement without load.

Table 1. CISPR25 class3-peak limits for conducted disturbances.

Service Band	Frequency/MHz	Limit/dB (μv)
Broadcast	0.15–0.30	90
	0.53–1.80	70
	5.9–6.2	65
	41–88	46
	76–108	50
Mobile services	26–28	56
	30–54	56
	68–87	50

3. System Conducted Emission Analysis

3.1. Noise Source

Figure 1 shows the circuit of a full bridge IGBT-based inverter in the motor controller model. The DC-fed PWM power inverter is designed to have a rated 250 V output voltage. The DC bus input voltage is 330 V. The six switches S_1–S_6 in the inverter are 1200 V/600 A full bridge IGBT modules (Infineon) with sinusoidal pulse width-modulation (SPWM) control. Although control methods (like space vector pulse width modulation (SVPWM), direct torque control (DTC), indirect field oriented control (IFOC), etc.) have better characteristics for mitigating harmonics, this is not the case for the EMI noise at high frequency. Therefore, we focus on the effect of characteristics of the trapezoidal wave for PWM on the EMI. We just take SPWM as an example for explaining the principle of the spectrum of the trapezoidal wave. The switching frequency of IGBT was set to 20 kHz and the line frequency for the AC motor was 400 Hz. The SPWM control signals are generated by compared a sinusoidal reference with a 20 kHz triangular carrier signal as illustrated in Figure 4a, which shows the PWM waveforms in a half-period, which have nine duty cycles corresponding to nine pulses with different pulse-widths. The noise source due to the SPWM control is often simplified by assuming a trapezoidal shape for the switching transients [26]. Each PWM pulse can be described as a trapezoidal pulse by an amplitude A, a frequency f, a pulse rise-time τ_r, a pulse fall-time τ_f and a pulse-wide τ. T represents the period of the trapezoidal pulse. The continuous envelope spectrum for a trapezoidal pulse can be given by the following equations [31]:

$$\text{Envelope} = 2\text{A}\frac{\tau}{\text{T}}\left|\frac{\sin(\pi\tau f)}{\pi\tau f}\right|\left|\frac{\sin(\pi\tau_r f)}{\pi\tau_r f}\right| \tag{1}$$

$$\begin{aligned} 20\log_{10}(\text{envelope}) = {} & 20\log_{10}(2\text{A}\tfrac{\tau}{T}) + 20\log_{10}(\tfrac{\sin(\pi\tau f)}{\pi\tau f}) \\ & +20\log_{10}(\tfrac{\sin(\pi\tau_r f)}{\pi\tau_r f}) \end{aligned} \tag{2}$$

The τ is smaller under unloaded operation conditions than that under load operation by SPWM control, as shown in Figure 4. Then from (1) and (2) the magnitude of the EMI noise voltage decreases as the value of τ decreases, and is lower under unloaded operation than that under load operation. From (1) and (2), the first break point in the frequency spectral bound is related to τ and is $1/\pi\tau$. The higher the τ, the wider the span related to the DC term, as shown in Figure 4b. The τ is smaller under unloaded operation conditions. Then the magnitude of the EMI noise voltage is lower under unloaded operation than that under load operation, as shown in Figure 3. The second breakpoint in the frequency spectral bound is related to rise/fall time and is $1/\pi\tau_r$.The smaller the rise/fall time, the larger the high-frequency spectral content, as shown in Figure 4c. The frequency band of the EMI noise source due to IGBT switching is from 0 Hz to 1 GHz. Then the resonances could be caused up to 1 GHz by parasitic distributed parameters of the AC motor system and may result in peak voltages exceeding the limit levels specified in the CISPR25 standard, as shown in Table 1.

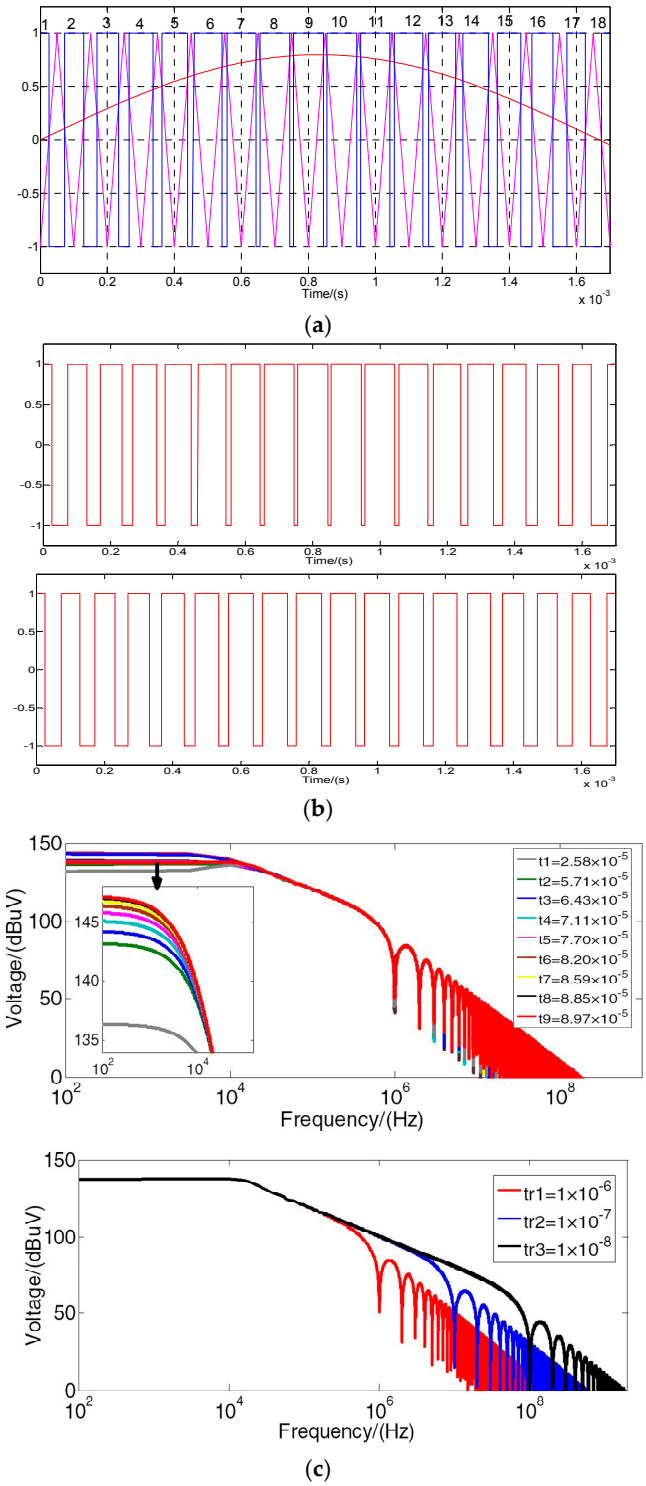

Figure 4. Spectral bounds for a trapezoidal wave: (**a**) SPWM in half-period; (**b**) The effect of pulse-width; (**c**) The effect of rise-time.

3.2. Analysis of the Current Path of Conducted Emissions

The self-inductance and mutual inductance are equivalent to one inductance in order to simplify the equivalent circuit for analyzing EMI propagation path. The motor drive system is constructed in DM and CM situation, as shown in Figure 5 and Figure 7, where, S_1–S_6 represent six IGBTs in the inverter, C_1–C_6 represent the distributed capacitance between the collector and emitter of S_1–S_6,

C_{Y1} and C_{Y2} represent the filter Y capacitors between the positive/negative DC cable and chassis, L_{Y1} and L_{Y2} represent the equivalent series inductances (ESLs) of C_{Y1} and C_{Y2}, C_X represents the filter X capacitor between the DC buses, L_X represents the equivalent series resistance (ESR) of C_X. Two LISNs can be represented by the circuit composed of R_{L1}, C_{L1}, R_{L2}, C_{L2}, C_7, C_8 and C_9 to represent the distributed capacitance from the collector and emitter of the IGBT to the chassis, C_{10} represents the distributed capacitance between the motor and the chassis. L_M represents the inductance of the motor phase winding, $L_{DC\ bus\ bar+}$ and $L_{DC\ bus\ bar-}$ represent the DC bus bars' inductance, which includes self-inductance and mutual inductance between two DC bus bars, so its value is larger than that of the lead stray inductance of IGBT, which is smaller and can be ignored, compared the inductance of the DC bus bars. C_{DC+} and C_{DC-} represent the DC cables' capacitance, L_{DC+} and L_{DC-} represent the DC cables' inductance, R_{DC1} and R_{DC2} represent the DC cables' resistance. The main distributed parameters' values are measured by VNA and shown in Table 2. The EMI noise propagation paths based on distributed parameters and the equivalent circuits of DM and CM noise current are respectively presented as follows.

Table 2. Parameters in the motor drive system.

Parameter	Value	Parameter	Value
L_{Y1}, L_{Y2}	200 nH	C_X	1028 μF
C_7	30 pF	L_X	20 nH
C_8	20 pF	C_1–C_6	20 pF
C_9	20 pF	R_{L1}, R_{L2}	50 Ω
C_{10}	200 pF	C_{L1}, C_{L2}	0.47 μF
C_{Y1}, C_{Y2}	100 pF	L_M	1 mH
L_{DC+}, L_{DC-}	50 nH	C_{DC+}, C_{DC-}	100 nF
R_{DC+}, R_{DC-}	0.0002 Ω	$L_{DC\ bus\ bar+}$, $L_{DC\ bus\ bar-}$	104 nH

3.2.1. Analysis of the DM Current Path for 500 kHz

The DM EMI emission from the phase node P between the two IGBTs of one phase bridge leg can be equivalent to a DM noise current source I_{DM} between the phase node P and DC bus minus the distributed parameters of the inner elements of the motor system, as shown in Figure 5a. The DM current loop can be illustrated by calculating the impedance of each circuit element ignoring the distributed parameters at 500 kHz, so the DM current flows though the distributed parameters of the motor system is shown in Figure 5b. I_{DM} acts as a driving force to form the following three current loops:

- current loop I: I_{DM}→C_4→$L_{DC\ bus\ bar-}$→R_{DC2}→L_X→C_X→R_{DC1}→$L_{DC\ bus\ bar+}$→C_1→I_{DM}
- current loop II: I_{DM}→L_M→C_6→$L_{DC\ bus\ bar-}$→R_{DC2}→L_X→C_X→R_{DC1}→$L_{DC\ bus\ bar+}$→C_1→I_{DM}
- current loop III: I_{DM}→L_M→C_2→$L_{DC\ bus\ bar-}$→R_{DC2}→L_X→C_X→R_{DC1}→$L_{DC\ bus\ bar+}$→C_1→I_{DM}

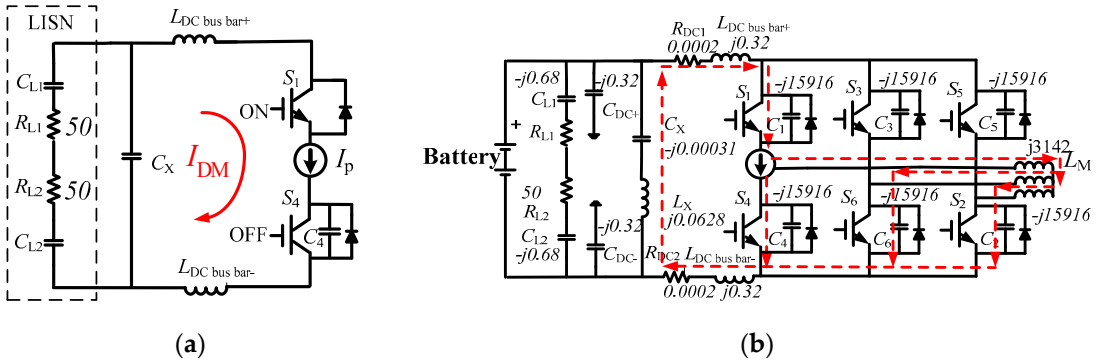

Figure 5. (**a**) Equivalent circuit for DM; (**b**) DM interference propagation path at 500 kHz.

3.2.2. Analysis of DM Current Path for 30 MHz

The impedance of each circuit element at 30 MHz is calculated as shown in Figure 6. I_{DM} acts as a driving force to form the following three current loops at 30 MHz:

- current loop I: $I_{DM} \rightarrow C_4 \rightarrow L_{DC\ bus\ bar-} \rightarrow R_{DC2} \rightarrow L_X \rightarrow C_X \rightarrow R_{DC1} \rightarrow L_{DC\ bus\ bar+} \rightarrow C_1 \rightarrow I_{DM}$
- current loop II: $I_{DM} \rightarrow C_4 \rightarrow C_6 \rightarrow C_3 \rightarrow C_1 \rightarrow I_{DM}$
- current loop III: $I_{DM} \rightarrow C_4 \rightarrow C_2 \rightarrow C_5 \rightarrow C_1 \rightarrow I_{DM}$

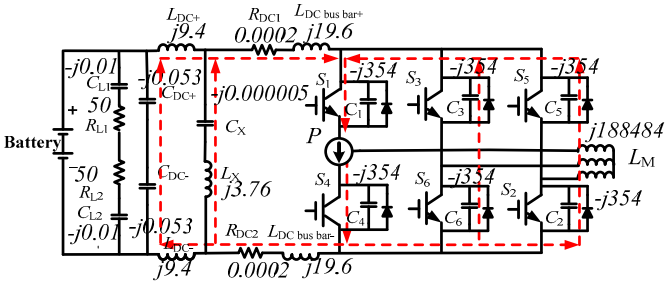

Figure 6. DM interference propagation path at 30 MHz.

The harmonic content of the DM current at 500 kHz and 30 MHz flowing through the 50 Ω impedance of LISN is also very small due to the filtering effect of the X capacitor. Then the resonant peak at about 500 kHz and 30 MHz is not dominated by the DM current.

3.2.3. Analysis of CM Current Path for 500 kHz

The CM noise current is always generated at high frequency and flows through the distributed parameters to the ground [32]. The CM emission from the phase node P of two IGBTs of one phase bridge leg can be equivalent to a CM voltage source U_{DM} between the phase node P and chassis with ignored distributed parameters of inner elements of the motor system, as shown in Figure 7a,b. The CM current loop can be illustrated by calculating the impedance of each circuit element with distributed parameters at 500 kHz. U_{CM} acts as a driving force to form three CM current loops shown in Figure 7c, where current loop1 (red line), current loop2 (blue line) and current loop3 (purple line) are considered in parallel. The CM current flowing paths at 500 kHz are composed of a DC side path and an AC side path. The effective impedance of inductance for one branch of the current loop (red) dominated by $L_{DC\ bus\ bar+}$ or $L_{DC\ bus\ bar-}$ is about j0.32 Ω and the effective impedance of capacitance for one branch of the current loop (red) dominated by the DC cable capacitance is about −j0.32 Ω. Therefore the peak voltage at about 500 kHz is mainly caused by the series resonance in the current loop (red).

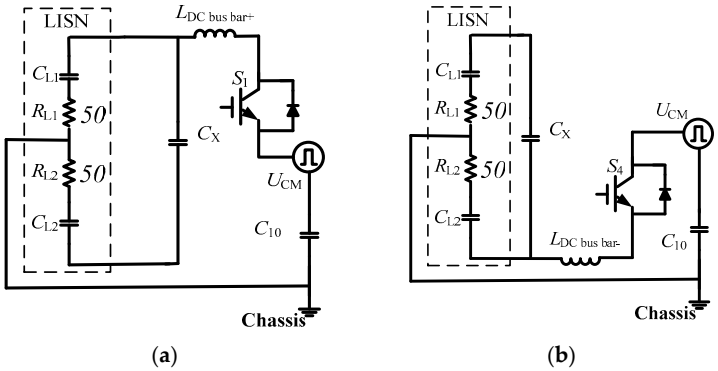

Figure 7. *Cont.*

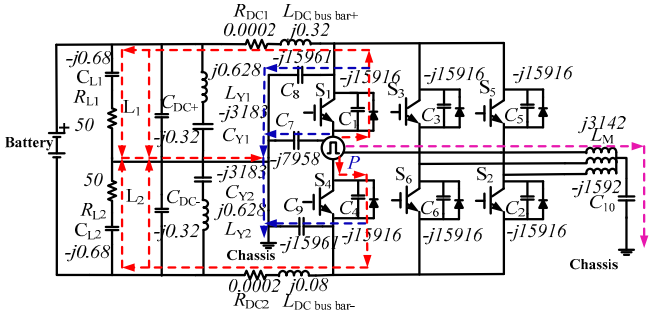

(**c**)

Figure 7. (**a**) Equivalent circuit for CM; (**b**) Equivalent circuit for CM; (**c**) CM interference propagation path at 500 KHz.

The elements responsible for the resonance at 500 kHz mainly are the capacitance between the DC cables and the chassis, and the stray inductance of the DC bus bar of IGBT. The resonance peak at about 500 kHz is mainly dominated by the CM current. The effect of the current loop2 (blue line) and current loop3 (purple line) is smaller and can be ignored in the equivalent circuit of CM current at 500 kHz shown in Figure 8.

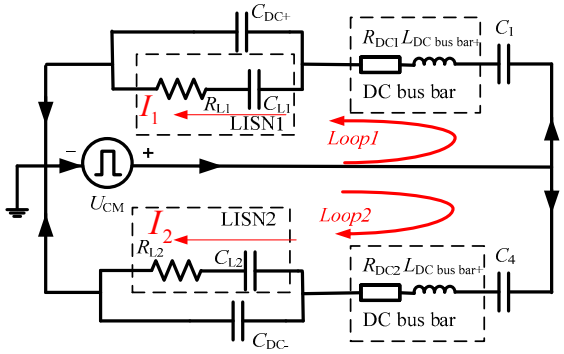

Figure 8. Equivalent circuit of CM interference at 500 KHz.

The CM current at about 500 kHz flowing on LISN can be expressed by the following equation:

$$I_1 = \frac{Z_1 U_{CM}}{(Z_1 + Z_2) Z_3} \lim_{x \to \infty} \tag{3}$$

where Z_1 denotes series-parallel impedance of R_{L1}, C_{L1} and C_{DC+}, Z_2 denotes series impedance of $L_{DC\ bus\ bar+}$, R_{DC1} and C_1, Z_3 denotes the series impedance of R_{L1} and C_{L1}.

3.2.4. Analysis of CM Current Path for 30 MHz

U_{DM} acts as a driving force to form the CM current loops shown in Figure 9. It is difficult to determine the main CM current loop and the elements responsible for the resonance at 30 MHz because of the complexity of CM current equivalent circuit dominated by C_1, C_4, $L_{DC\ bus\ bar+}$, $L_{DC\ bus\ bar-}$, R_{DC2}, R_{DC1}, R_{DC2}, L_{DC+}, L_{DC-}, C_{Y1}, L_{Y1}, C_{Y2}, L_{Y2}, C_7, C_8 and C_9. The model of the CM current equivalent circuit is essential to study the main dominated CM current loop at 30 MHz to determine the distributed parameters responsible for the resonance peak at 30 MHz.

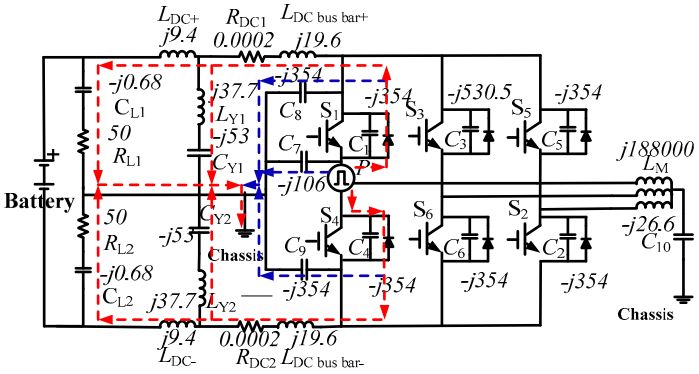

Figure 9. CM interference propagation path at 30 MHz.

The equivalent circuit of CM current at 30 MHz is shown in Figure 10 and the CM current at 30 MHz flowing through the LISN resistor can be expressed by the following equation:

$$I_2 = \frac{Z_1 U_{CM}}{(Z_1 + Z_{C1})(Z_2 + Z_3)Z_4} \tag{4}$$

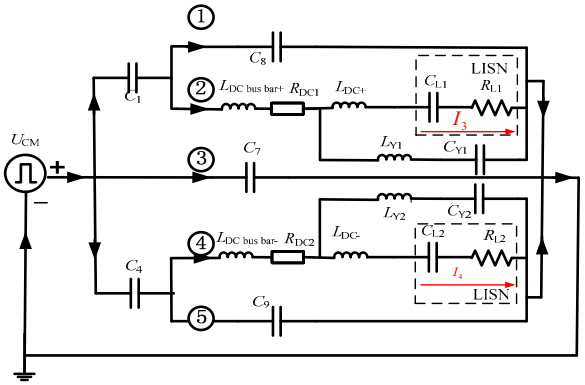

Figure 10. Equivalent circuit of CM interference at 30 MHz.

Z_1 denotes series-parallel impedance of C_8, $L_{DC\ bus\ bar+}$, R_{DC1}, L_{DC+}, C_{Y1}, L_{Y1}, C_{L1} and R_{L1}. Z_2 denotes series impedance of $L_{DC\ bus\ bar+}$ and R_{DC1}. Z_3 denotes series-parallel impedance of L_{DC+}, C_{L1}, R_{L1}, C_{Y1} and L_{Y1}. Z_4 denotes series impedance of L_{DC+}, C_{L1} and R_{L1}.

From Equation (3), C_{DC+}, $L_{DC\ bus\ bar+}$, C_{DC-} and $L_{DC\ bus\ bar-}$ are the dominant distributed parameters causing the series resonance at 500 kHz and the effect on the CM current I_1. Therefore C_1 and C_4 have a very small effect on I_1 and can be ignored. Changing of any parameter among C_{DC+}, $L_{DC\ bus\ bar+}$, C_{DC-} and $L_{DC\ bus\ bar+}$ can reduce the value of I_1 at 500 kHz. From Equation (4), L_{DC+}, C_{Y1}, L_{Y1}, L_{DC-}, C_{Y2}, L_{Y2}, C_8 and C_9 are the effective distributed parameters at 30 MHz and with an effect on I_1.

The effect from distributed parameters on conducted voltage U_R according to above equivalent circuits and calculation at 500 kHz and 30 MHz is shown in Table 3. In a motor drive system, the parameters such as C_1–C_6, C_X, L_X and L_M usually cannot be controlled, and only the distributed parameters $L_{DC\ bus\ bar+}$, $L_{DC\ bus\ bar-}$, C_{DC+}, C_{DC-}, C_8, C_9, L_{Y1}, L_{Y2}, C_{Y1}, C_{Y2} could be changed along with different arrangements, filtering and shielding.

Table 3. The effect of the main distribution parameter on conducted EMI emission.

Changing of Parameters	Current	Voltage
$L_{\text{DC bus bar+}} \uparrow$ or $\downarrow$	$I_1 \downarrow$	$U_R \downarrow$
$L_{\text{DC bus bar}-} \uparrow$ or $\downarrow$	$I_1 \downarrow$	$U_R \downarrow$
$C_{DC+} \uparrow$ or $\downarrow$	$I_1 \downarrow$	$U_R \downarrow$
$C_{DC-} \uparrow$ or $\downarrow$	$I_1 \downarrow$	$U_R \downarrow$
$C_8 \uparrow$	$I_2 \downarrow$	$U_R \downarrow$
$C_9 \uparrow$	$I_2 \downarrow$	$U_R \downarrow$
$L_{Y1} \uparrow$	$I_2 \downarrow$	$U_R \downarrow$
$L_{Y2} \uparrow$	$I_2 \downarrow$	$U_R \downarrow$
$C_{Y1} \uparrow$	$I_2 \downarrow$	$U_R \downarrow$
$C_{Y2} \uparrow$	$I_2 \downarrow$	$U_R \downarrow$
$L_{\text{DC bus bar+}} \uparrow$	$I_2 \downarrow$	$U_R \downarrow$
$L_{\text{DC bus bar}-} \uparrow$	$I_2 \downarrow$	$U_R \downarrow$

4. Simulation of the Effect of Distributed Parameters

4.1. System Conducted EMI Modeling

According to the structure of the system and the distributed parameters, the power inverter system was modeled as a simplified single-arm bridge of the power inverter system using the EMC simulation software "Computer Simulation Technology" (CST) that predicts the noise in the entire conducted emissions range from 150 kHz to 108 MHz, as illustrated in Figure 11. The conducted emission (CE) voltage on the resistor of the LISN in the DM and CM network equivalent circuits can be obtained by using time-domain simulation, followed by fast fourier transform(FFT) in the designer platform provided in the CST software. The CM EMI source is equivalent to an ideal trapezoidal shape wave and the EMI voltage measured by a probe P_1 is the positive conducted emission voltage. The EMI voltage simulation result is shown in Figure 12. Table 3 and Figure 12 suggest that the conducted EMI voltage spectrum of the motor drive system in EV can be divided into two different frequency ranges: the low frequency range around 500 kHz that is dominated by DC cables' capacitance and DC bus bars, and the high frequency range around 30 MHz that is related to parasitic resonances due to the distributed parameters of Y capacitors and distributed capacitance from the IGBT phase node to the chassis. The EMI voltage peaks obtained through simulation in Figure 12 correspond to those of measurements at 500 kHz and 30 MHz. There are some larger errors between simulation results and measurement results because the measurement EMI voltage is the total of the EMI noise from the three arms of the power inverter. Conversely, the simulated EMI voltage is obtained from a single-arm. It can be seen that the model is efficient enough to be used to predict the CM current paths and the elements responsible for the EMI.

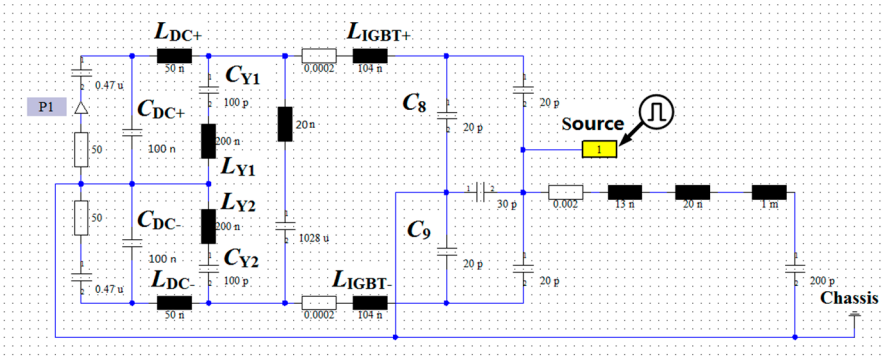

Figure 11. CM circuit model of single-arm bridge of power inverter.

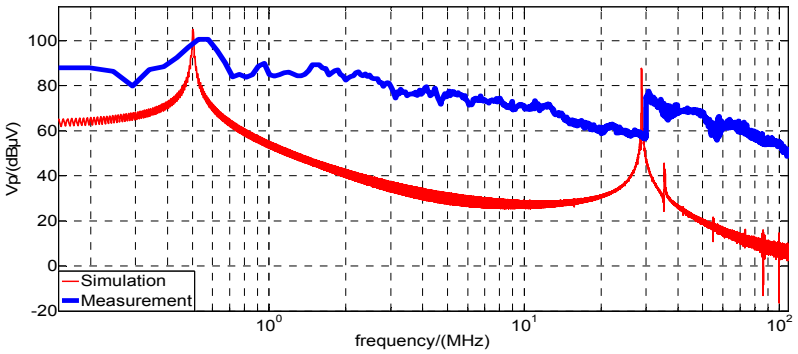

Figure 12. Comparison of measurement and simulation.

4.2. The Effect of Distributed Parameters

4.2.1. The Effect of $L_{\text{DC bus bar+}}$ and $L_{\text{DC bus bar}-}$

According to Table 3, changing the value of $L_{\text{DC bus bar+}}$ and $L_{\text{DC bus bar}-}$ can mitigate the resonance and reduce the conducted emissions at low frequency. Therefore, the EMI voltage peak due to resonance at 500 kHz could be suppressed. The voltage value of conducted emission at 500 kHz can be rapidly decreased by about 50 dB by increasing the value of $L_{\text{DC bus bar+}}$ and $L_{\text{DC bus bar}-}$ from 104 nH to 220 nH to comply with the limit level-3 of CISPR25 regulatory standards, as shown in Figure 13. It suggests that two CM inductors can be placed on the DC bus bar of the power inverter of the AC motor to reduce the CM current and conducted emission at 500 kHz.

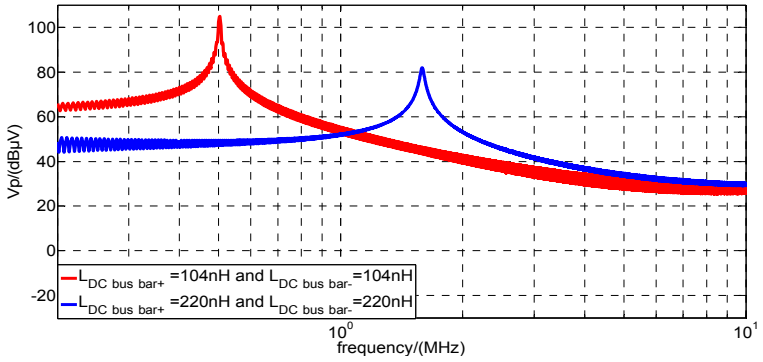

Figure 13. Positive conducted emission(CE) voltage after $L_{\text{DC bus bar+}}$ and $L_{\text{DC bus bar}-}$ were increased.

4.2.2. The Effect of L_{Y1} and L_{Y2}

According to Table 3, L_{Y1} and L_{Y2} can be increased to mitigate the resonance and reduce the conducted emission at high frequency. Therefore, the EMI voltage peak due to resonance at 30 MHz could be suppressed. The voltage value of conducted emission at 30 MHz can be rapidly decreased by about 64 dB by increasing the value of L_{Y1} and L_{Y2} from 200 nH to 300 nH to comply with the level-3 limit of CISPR25, as shown in Figure 14. It suggests that the equivalent series inductance of Y capacitor can affect the conducted EMI at 30 MHz. A better design of the parameters of the Y capacitor can reduce the conducted emissions at high frequency.

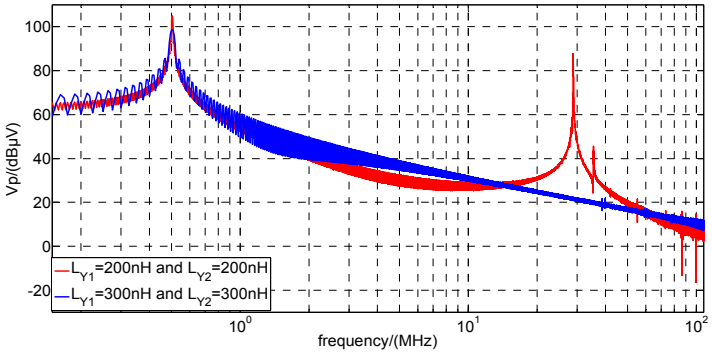

Figure 14. Positive CE voltage after L_{Y1} and L_{Y2} were increased.

4.2.3. The Effect of Combination of $L_{DC\ bus\ bar+}$, $L_{DC\ bus\ bar-}$, L_{Y1} and L_{Y2}

Increasing of the value of $L_{DC\ bus\ bar+}$, $L_{DC\ bus\ bar-}$ (each 220 nH) and L_{Y1}, L_{Y2} (each 300 nH) can decrease the conduced emissions at frequencies from 150 kHz to 108 MHz to below the limit level-3 of CISPR25. Then there are no resonances previously caused by $L_{DC\ bus\ bar+}$ and $L_{DC\ bus\ bar-}$ at 500 kHz, L_{Y1} and L_{Y2} at 30 MHz. Although there still is a resonance point at around 55 MHz, the value of conducted voltage is decreased below the level-3 limit of CISPR25, as shown in Figure 15.

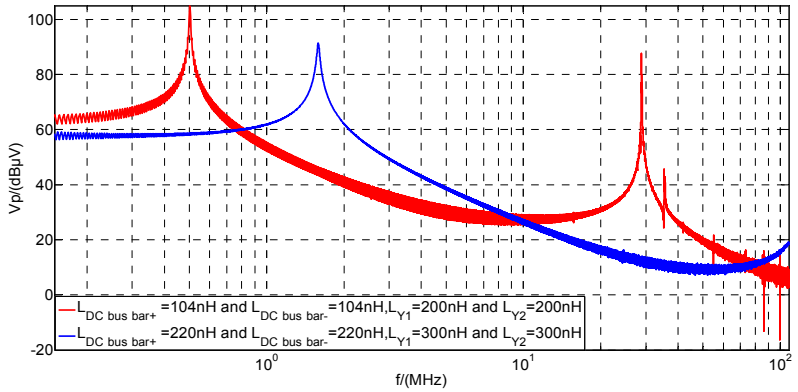

Figure 15. Positive CE voltage after $L_{DC\ bus\ bar+}$, $L_{DC\ bus\ bar-}$, L_{Y1} and L_{Y2} were increased.

4.2.4. The Effect of C_{DC+} and C_{DC-}

From Table 3, the distributed capacitances from DC cables (C_{DC+}, C_{DC-}) can affect the conducted emissions. Changing the value of C_{DC+} and C_{DC-} can mitigate the resonance at 500 kHz and reduce the conducted emission at low frequency. The voltage value of conducted emission at 500 kHz can be decreased by about 25 dB by increasing the value of C_{DC+} and C_{DC-} from 100 nF to 250 nF to comply with the limit level-3 of CISPR25, as shown in Figure 16. It suggests that filtering and shielding of the DC input of the power inverter of the AC motor can be used to change the distributed parameters of DC cables to reduce the CM current at low frequency and suppress the EMI voltage peak due to resonance at 500 kHz. For example, a Y capacitor could be added between the DC cable and chassis to reduce conducted emissions, although the Y capacitor may cause a high ground leakage current.

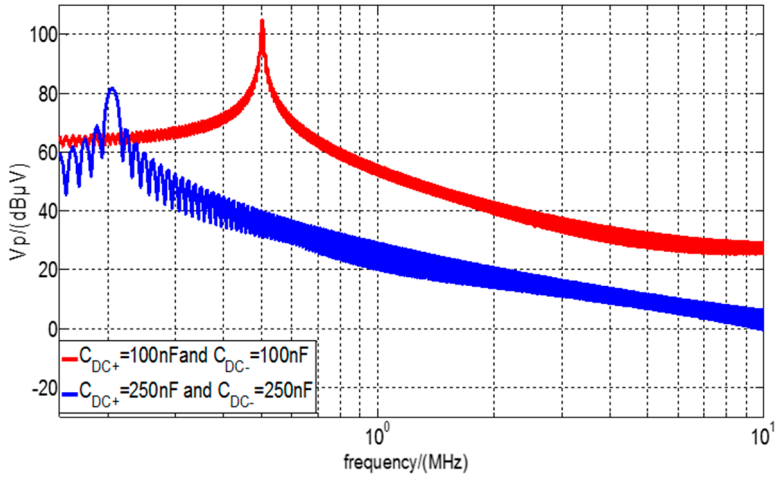

Figure 16. Positive CE voltage after C_{DC+} and C_{DC-} were increased.

4.2.5. The Effect of the Combination of C_{Y1}, C_{Y2}, C_8 and C_9

From Table 3, the capacitances of the Y capacitors (C_{Y1}, C_{Y2}) and the distributed capacitance from the collector and emitter of the IGBT to the chassis (C_8, C_9) can affect the conduced emissions at high frequency. The voltage value of conducted emissions at high frequency can be decreased to comply with CISPR25 by increasing the value of C_{Y1} and C_{Y2} from 100 nF to 500 nF and the value of C_8 and C_9 from 20 pF to 100 pF, as shown in Figure 17. It shows that the peak value of the conducted voltage is reduced by 20 dB at about 30 MHz. Therefore, Y capacitors could be added between the collector and emitter of the IGBT and chassis, and between DC input and chassis to reduce conducted emissions at high frequency.

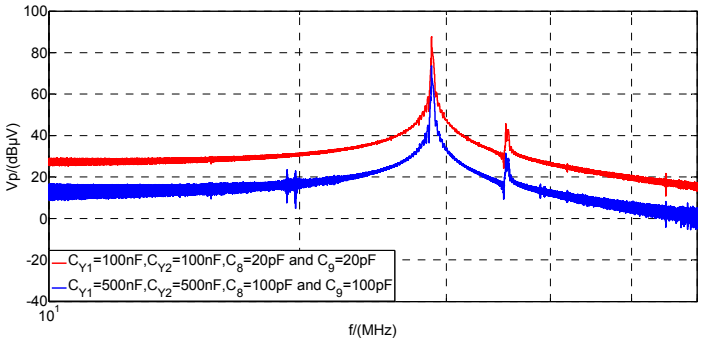

Figure 17. Positive CE voltage after C_{Y1}, C_{Y2}, C_8 and C_9 were increased.

4.2.6. The Effect of the Combination of C_{DC+}, C_{DC-}, C_{Y1}, C_{Y2}, C_8 and C_9

It is a better mitigation method to change the value of the distributed parameters (C_{DC+}, C_{DC-}, C_{Y1}, C_{Y2}, C_8 and C_9) to reduce the conducted emission at frequencies from 150 kHz to 108 MHz defined in CISPR25. The conducted voltage is reduced by increasing the capacitances (C_{DC+} = C_{DC-} = 250 nF, C_{Y1} = C_{Y2} = 500 nF, C_8 = C_9 = 100 pF), as shown in Figure 18.

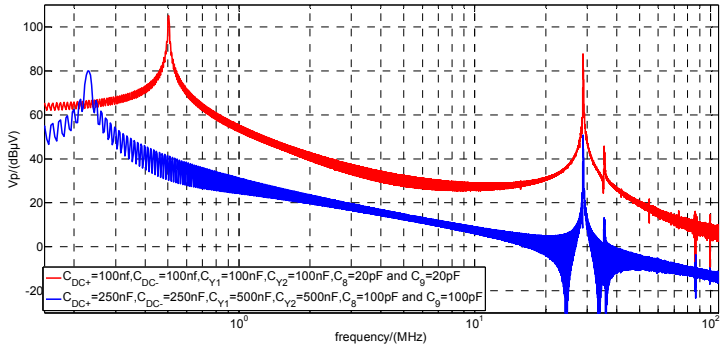

Figure 18. Positive CE voltage after C_{DC+}, C_{DC-}, C_{Y1}, C_{Y2}, C_8 and C_9 were increased.

5. Experimental Verification

According to the above analysis of the effect of distributed parameters on the power inverter system of AC motors for EVs, changing the combination of C_{DC+}, C_{DC-}, C_{Y1}, C_{Y2}, C_7 and C_8 should be a better way to suppress the voltage peak at 500 kHz and 30 MHz to comply with the limit level-3 of CISPR 25. A new pair of Y capacitors are added between the collector and emitter of the IGBT and DC bus bar and the chassis to increase the capacitances between the inverter and the chassis. Experimental verification is conducted and the results are shown in Figure 19. The conducted emission characteristics at around 500 kHz and 30 MHz in Figure 19 are approximately as predicted by the simulation in Figure 18.

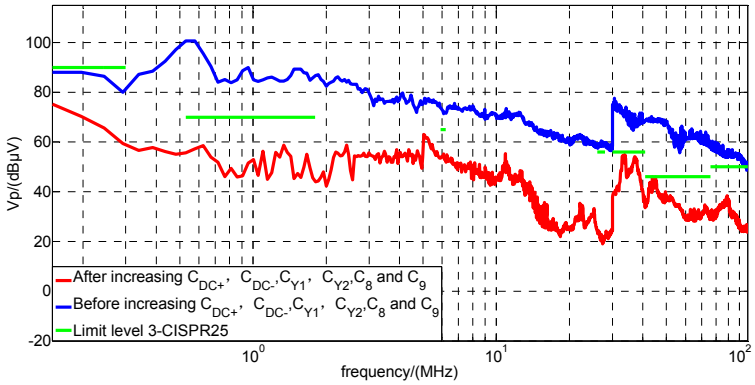

Figure 19. Positive CE voltage after C_{DC+}, C_{DC-}, C_{Y1}, C_{Y2}, C_8 and C_9 were increased.

6. Conclusions

This study proposed a new method to analyze the effects of distributed parameters on conducted EMI from the DC-fed high voltage motor drive systems in EVs. The conducted EMI of high voltage DC cables of the motor drive system in a frequency range of 150 kHz–108 MHz and two EMI noise peaks at resonances frequencies 500 kHz and 30 MHz have been measured by a complete test for conducted EMI emissions from the AC motor drive system of an EV under load conditions. The research mainly focuses on the effects of distributed parameters in the inverter and cables on the resonances at 500 kHz and 30 MHz, nor the distributed parameters of the motor due to the high impedance of the motor model at 500 kHz and 30 MHz. The corresponding equivalent circuits for DM and CM EMI at resonance frequencies of 500 kHz and 30 MHz are established to determine the EMI propagation paths and the dominant distributed parameters of elements responsible for the resonances appearing at 500 kHz and 30 MHz.

The distributed parameters $L_{DC\ bus\ bar+}$, $L_{DC\ bus\ bar-}$, C_{DC+}, C_{DC-}, C_8, C_9, L_{Y1}, L_{Y2}, C_{Y1} and C_{Y2} can affect the EMI emissions from the high voltage motor drive system. The effect of the dominant

distributed parameters on conducted voltage is verified by modeling of the CM circuit of a single-arm bridge of the high voltage motor power inverter. Increasing the value of $L_{\text{DC bus bar+}}$, $L_{\text{DC bus bar}-}$ from 104 nH to 220 nH and L_{Y1}, L_{Y2} from 200 nH to 300 nH or increasing the capacitances ($C_{\text{DC+}}$, $C_{\text{DC}-}$ from 100 nF to 250 nF, C_{Y1}, C_{Y2} from 100 nF to 500 nF, C_8, C_9 from 20 pF to 100 pF) can mitigate the two resonance peaks at the frequencies of 500 kHz and 30 MHz and decrease the conduced voltage at frequencies from 150 kHz to 108 MHz to below the limit level-3 of CISPR25. The effect of the combination of $C_{\text{DC+}}$, $C_{\text{DC}-}$, C_{Y1}, C_{Y2}, C_8 and C_9 on conducted voltage is verified by experiments. In future work, modeling of a CM circuit of three-arm bridge of the high voltage motor power inverter in EV will be developed. After that the effect of distributed parameters on EMI noise will be further simulated and tested.

Acknowledgments: This study is supported by National Natural Science of Foundation of China and Outstanding Talents Project of Beijing.

Author Contributions: Li Zhai analyzed the system conducted emission; Liwen Lin and Xinyu Zhang performed the modeling; Li Zhai and Chao Song performed the experiments; Li Zhai and Liwen Lin analyzed the data; Li Zhai wrote the paper.

Conflicts of Interest: The authors declare no conflict of interest.

References

1. Sun, F.; Xiong, R.; He, H. A systematic state-of-charge estimation framework for multi-cell battery pack in electric vehicles using bias correction technique. *Appl. Energy* **2016**, *162*, 1399–1409. [CrossRef]
2. Ferrero, E.; Alessandrini, S.; Balanzino, A.; Yan, J. Impact of the electric vehicles on the air pollution from a highway. *Appl. Energy* **2016**, *169*, 450–459. [CrossRef]
3. Hu, X.; Murgovski, N.; Johannesson, L.; Bo, E. Energy efficiency analysis of a series plug-in hybrid electric bus with different energy management strategies and battery sizes. *Appl. Energy* **2013**, *111*, 1001–1009. [CrossRef]
4. Chen, Z.; Xiong, R.; Wang, C.; Cao, J. An on-line predictive energy management strategy for plug-in hybrid electric vehicles to counter the uncertain prediction of the driving cycle. *Appl. Energy* **2016**, *185*, 1663–1672. [CrossRef]
5. Torresa, J.L.; Gonzalezb, R.; Gimeneza, A.; Lopeza, J. Energy management strategy for plug-in hybrid electric vehicles. A comparative study. *Appl. Energy* **2014**, *113*, 816–824. [CrossRef]
6. Zhai, L.; Zhang, X.; Bondarenko, N.; Loken, D.; Doren, T.V.; Beetner, D.G. Mitigation emission strategy based on resonances from a power inverter system in electric vehicles. *Energies* **2016**, *9*, 419. [CrossRef]
7. Ehsani, M.; Gao, Y.; Emadi, A. *Modern Electric, Hybrid Electric, and Fuel Cell Vehicles: Fundamentals, Theory, and Design*; CRC Press: Boca Raton, FL, USA, 2010.
8. Ardon, V.; Aime, J.; Chadebec, O.; Clavel, E. EMC modeling of an industrial variable speed drive with an adapted PEEC method. *IEEE Trans. Magn.* **2010**, *46*, 2892–2898. [CrossRef]
9. Lai, J.S.; Huang, X.; Chen, S.; Nehl, T.W. EMI characterization and simulation with parasitic models for a low-Voltage high-current AC motor drive. *IEEE Trans. Ind. Appl.* **2004**, *40*, 178–185. [CrossRef]
10. Jettanasen, C.; Costa, F.; Vollaire, C. Common-mode emissions measurements and simulation in variable-speed drive systems. *IEEE Trans. Power Electron.* **2009**, *24*, 2456–2464. [CrossRef]
11. Tommasini, R.; Spertino, F. Electric power distribution and environment: Interference of power installation magnetic fields on computer systems. *Appl. Energy* **1999**, *64*, 181–193. [CrossRef]
12. Toure, B.; Schanen, J.-L.; Gerbaud, L.; Meynard, T.; Roudet, J.; Ruelland, R. EMC modeling of drives for aircraft applications: Modeling process, EMI filter optimization and technological choice. *IEEE Trans. Power Electron.* **2013**, *28*, 1145–1156. [CrossRef]
13. Lai, J.S. Resonant snubber-based soft-switching inverters for electric propulsion drives. *IEEE Trans. Ind. Electron.* **1997**, *44*, 71–80.
14. Mutoh, N.; Ogata, M. New methods to control EMI noises generated in motor drive systems. *IEEE Trans. Ind. Appl.* **2004**, *40*, 143–152. [CrossRef]
15. Rebholz, H.M.; Tenbohlen, S.; Kohler, W. Time-domain characterization of RF sources for the design of noise suppression filters. *IEEE Trans. Electromagn. Compat.* **2009**, *51*, 945–952. [CrossRef]

16. Reuter, M.; Friedl, T.; Tenbohlen, S.; Köhler, W. Emulation of conducted emissions of an automotive inverter for filter development in HV networks. In Proceedings of the IEEE International Symposium on Electromagnetic Compatibility (EMC), Denver, CO, USA, 5–9 August 2013; pp. 236–241.
17. Trzynadlowski, A.M.; Wang, Z.; Nagashima, J.; Stancu, C. Comparative investigation of PWM techniques for general motor's new drive for electric vehicles. In Proceedings of the IEEE Industry Applications Conference, Pittsburgh, PA, USA, 13–18 October 2002; pp. 2010–2015.
18. Piazza, M.C.D.; Ragusa, A.; Tine, G.; Vitale, G. A model of electromagnetic radiated emissions for dual Voltage automotive electrical systems. In Proceedings of the IEEE International Symposium on Industrial Electronics, Ajaccio, France, 4–7 May 2004; pp. 317–322.
19. Akagi, H.; Shimizu, T. Attenuation of conducted EMI emissions from an inverter-driven motor. *IEEE Trans. Power Electron.* **2008**, *23*, 282–290. [CrossRef]
20. Wang, S.; Maillet, Y.Y.; Wang, F.; Lai, R.; Luo, F.; Boroyevich, D. Parasitic effects of grounding paths on common-mode EMI filter's performance in power electronics systems. *IEEE Trans. Ind. Electron.* **2010**, *57*, 3050–3059. [CrossRef]
21. Bishnoi, H.; Baisden, A.C.; Mattavelli, P.; Boroyevich, D. Analysis of EMI terminal modeling of switched power converters. *IEEE Trans. Power Electron.* **2012**, *27*, 3924–3933. [CrossRef]
22. Gong, X.; Ferreira, A.J. Comparison and reduction of conducted EMI in SiC JFET and Si IGBT-based motor drives. *IEEE Trans. Power Electron.* **2014**, *29*, 1757–1767. [CrossRef]
23. Revol, B.; Roudet, J.; Schanen, J.L.; Loizelet, P. EMI study of three-phase inverter-fed motor drives. *IEEE Trans. Ind. Appl.* **2011**, *47*, 223–231. [CrossRef]
24. Stevanovic, I.; Skibin, S.; Masti, M.; Laitinen, M. Behavioral modeling of chokes for EMI simulations in power electronics. *IEEE Trans. Power Electron.* **2013**, *28*, 695–705. [CrossRef]
25. Mutoh, N.; Ogata, M.; Gulez, K.; Harashima, F. New methods to suppress EMI noises in motor drive systems. *IEEE Trans. Ind. Electron.* **2002**, *49*, 474–485. [CrossRef]
26. Bishnoi, H.; Mattavelli, P.; Burgos, R.; Boroyevich, D. EMI behavioral models of DC-fed three-phase motor drive systems. *IEEE Trans. Power Electron.* **2014**, *29*, 4633–4645. [CrossRef]
27. Bondarenko, N.; Zhai, L.; Xu, B.; Li, G.; Makharashvili, T.; Loken, D.; Berger, P.; Doren, T.P.V.; Beetner, D.G. A measurement-based model of the electromagnetic emissions from a power inverter. *IEEE Trans. Power Electron.* **2015**, *30*, 5522–5531. [CrossRef]
28. Australia, S. *Vehicle, Boats and Internal Combustion Engines—Limits and Methods of Measurement for the Protection of on-Board Receivers*; CISPR25; International Special Committee on Radio Interference: Geneva, Switzerland, 2012.
29. Mihalic, F.; Kos, D. Reduced conductive EMI in switched-mode DC–DC power converters without EMI filters: PWM versus randomized PWM. *IEEE Trans. Power Electron.* **2006**, *21*, 1783–1794. [CrossRef]
30. Chen, S.; Nehl, T.W.; Lai, J.-S.; Huang, X.; Pepa, E.; de Doncker, R.; Voss, I. Towards EMI prediction of a PM motor drive for automotive applications. In Proceedings of the Applied Power Electronics Conference and Exposition, Miami Beach, FL, USA, 9–13 February 2003; pp. 14–22.
31. Paul, C.R. *Introduction to EMC*; Wiley & Sons. Inc.: New York, NY, USA, 1992; pp. 466–474.
32. Mugur, P.R.; Roudet, J.; Crebier, J.C. Power electronic converter EMC analysis through state variable approach techniques. *IEEE Trans. Electromagn. Compat.* **2001**, *43*, 229–238. [CrossRef]